



CrossMark
 click for updates

Cite this: *RSC Adv.*, 2016, 6, 20437

Microstructure, vibrational and visible emission properties of low frequency ultrasound (42 kHz) assisted ZnO nanostructures†

Thangaraj Pandiyarajan,^{*a} Ramalinga Viswanathan Mangalaraja,^{*a} Balasubramanian Karthikeyan,^b Selene Sepulveda-Guzman,^c Héctor D. Mansilla,^d David Contreras,^e Néstor Escalona^{f,g} and M. A. Gracia-Pinilla^{h,i}

Size and shape tuneable ZnO nanostructures were prepared by a low frequency ultrasound (42 kHz) route using various organic solvents as the reaction media. The crystalline nature, lattice parameters and microstructural parameters such as microstrain, stress and energy density of the prepared ZnO nanostructures were revealed through X-ray diffraction (XRD) analysis. The organic solvents influenced the size and morphology of the ZnO nanostructures, and interesting morphological changes involving a spherical to triangular shaped transition were observed. The visible emission properties and lattice vibrational characteristics of the nanostructures were drastically modified by the changes in size and shape. Raman spectral measurements revealed the presence of multiphonon processes in the ZnO nanostructures. The intensity of the visible emission band was found to vary with the size and morphology of the structures. The strongest visible emission band corresponded to the structure with the largest surface/volume ratio and could be attributed to surface oxygen vacancies. The control over the size and morphology of ZnO nanostructures has been presented as a means of determining the intensity of the visible emission band.

Received 18th December 2015
 Accepted 4th February 2016

DOI: 10.1039/c5ra27147a

www.rsc.org/advances

Introduction

Zinc oxide (ZnO) structures with different sizes and shapes have been the subject of numerous studies in recent decades because of their versatile properties.¹ In particular, the size of ZnO particles has been adjusted in order to tune the emission from

the band gap and defects.² This material shows interesting properties in the nanoscale region. In this region, ZnO is expected to possess novel physical and chemical properties compared to the respective bulk counterpart.³ Naturally, ZnO is a II–VI wide band gap semiconductor with a band gap of 3.37 eV and a high exciton binding energy (60 meV) at room temperature compared with other semiconductors in this family. ZnO has a wide range of applications in electronic and optoelectronic devices,⁴ solar cells,⁵ photodetectors^{6,7} and as an environmental material in photocatalysis,⁸ gas sensors⁹ and antibacterial activity.¹⁰ These properties are highly dependent on the particle size, morphology and surface area, and hence nanosized ZnO is receiving great attention because of its high surface area. ZnO nanostructures with different sizes and shapes exhibit promising properties particularly for applications in short wavelength optoelectronic devices and sensors. Several routes, such as solvothermal,¹¹ hydrothermal,¹² microwave,¹³ combustion¹⁴ and sonochemical,¹⁵ have been developed to synthesis ZnO nanostructures with different sizes and shapes. The preparations of different sized and shaped nanostructures are closely associated with different parameters such as pH,¹⁶ temperature,¹⁷ growth technique¹⁸ and solvent.¹⁹ There are numerous reports available in the literature of ZnO nanostructures with different sizes and shapes, but limited reports are available on the microstructural parameters which determine the optical properties of ZnO nanostructures. For

^aAdvanced Ceramics and Nanotechnology Laboratory, Department of Materials Engineering, University of Concepcion, Chile. E-mail: rtpandiyarjan@gmail.com; mangal@udec.cl; Fax: +56-41-2203391; Tel: +56-41-2207389

^bDepartment of Physics, National Institute of Technology, Tiruchirappalli 620 015, India

^cUniversidad Autónoma de Nuevo León UANL, Facultad de Ingeniería Mecánica y Eléctrica, FIME, Ave. Pedro de Alba s/n, Ciudad Universitaria, C. P. 66455, San Nicolás de los Garza, N. L., Mexico

^dDepartment of Organic Chemistry, Faculty of Chemical Sciences, University of Concepcion, Chile

^eDepartment of Analytical and Inorganic Chemistry, Faculty of Chemical Sciences, Center for Biotechnology, University of Concepcion, Chile

^fDepartment of Chemical and Bioprocess Engineering, School of Engineering, Catholic University of Chile, Macul, Avenida Vicuña Mackenna 4860, Santiago, Chile

^gFaculty of Chemistry, Pontifical Catholic University of Chile, Chile

^hUniversidad Autónoma de Nuevo León, Facultad de Ciencias Físico-Matemáticas, Av. Universidad, Cd. Universitaria, San Nicolás de los Garza, NL, Mexico

ⁱCentro de Investigación en Innovación y Desarrollo en Ingeniería y Tecnología, Universidad Autónoma de Nuevo León, PIIT, Apodaca, Nuevo León, 66600, Mexico

† Electronic supplementary information (ESI) available. See DOI: 10.1039/c5ra27147a

instance, Patete *et al.*²⁰ have published a detailed review on the viable methodologies for the synthesis of various kinds of nanostructures with different sizes and shapes for various applications. Ghosh *et al.*²¹ have reported the effects of size and aspect ratio on structural parameters in ZnO nanostructures. Recently, Chandraiahgari and his group²² have reported simple preparation techniques for the large-scale synthesis of ZnO nanorods with a narrow size distribution. Their results showed that the various process parameters, such as precursor amount and growth time, played an important role in controlling the formation of nanostructures with high uniformity in size and morphology. The effects of solvents on size, shape, and magnetic and photoluminescence properties of ZnO nanostructures have been reported by Clavel and his group,²³ Hu *et al.*²⁴ and Foo and colleagues.²⁵ Fang *et al.*²⁶ have reported a detailed study on the synthesis of one-dimensional inorganic semiconductor nanostructures for nanosensor applications. The shape dependence of the photoluminescence of ZnO nanocrystals was studied by Andelman *et al.*²⁷ Similarly, Ye *et al.*²⁸ have prepared various morphological ZnO nanostructures and have investigated, in detail, their morphology derivation and evolution. Enhanced photocatalytic activities of ZnO nanostructures with various morphologies synthesized with different organic solvents were studied by Pimentel *et al.*²⁹

Reports are available on the observation of anomalous modes in the Raman spectra which do not correspond to the first/second order Raman modes of undoped and doped wurtzite-ZnO nanostructures. For instance, the observation of disorder-activated anomalous Raman silent modes was reported by Manjon *et al.*³⁰ as well as Scepanovic and his co-workers.³¹ Cuscó *et al.*³² have reported a detailed investigation of Raman modes in high quality ZnO single crystals over a temperature range from 80 to 750 K. Yadav *et al.*³³ and Zeferino *et al.*³⁴ have identified that a dopant can induce the activation of Raman silent modes in ZnO nanostructures, due to the relaxation of Raman selection rules produced by the breakdown of the translational symmetry of the crystal lattice with the replacement of Zn in the lattice by the dopant ion. Kunert *et al.*³⁵ have done the detailed studies on the derivation of Raman selection rules for the multiphonon processes in ZnO lattices. However, to the best of our knowledge, a systematic investigation of solvent effects on microstructure and optical properties of ZnO nanostructures has not yet been reported.

Polar protic solvents achieve ZnO nanostructures with controlled size and high homogeneity. This is important for tuning the physical and chemical properties of nanoparticles, and especially for engineering the band gap and defect properties for optoelectronic device applications. Owing to the importance of ZnO nanostructures in various technological applications, size and morphology tuneable ZnO nanostructures were prepared in this report, by the low frequency ultrasonic (42 kHz) route using various polar protic solvents as the reaction media. An attempt was made to study the effects of the different organic solvents on the microstructure and presence of anomalous Raman modes. We also explored the visible emission properties of the nanostructures with respect to their size and shape, and the results are reported in detail.

Experimental

Materials

Zinc acetate dihydrate $\text{Zn}(\text{CH}_3\text{COO})_2 \cdot 2\text{H}_2\text{O}$, sodium hydroxide (NaOH), ethanol ($\text{CH}_3\text{CH}_2\text{OH}$), isopropanol ($\text{C}_3\text{H}_8\text{O}$), methanol (CH_3OH) and 1-butanol ($\text{C}_4\text{H}_9\text{OH}$) were purchased from Sigma-Aldrich. All the reactants were used as received without further purification. The molecular structures of these solvents are shown in ESI Fig. 1.†

Synthesis of ZnO nanostructures

Different sizes of ZnO nanostructures were prepared by low frequency ultrasound (42 kHz) using various organic solvents (ethanol, methanol, isopropanol and 1-butanol) and double distilled water, keeping all other reaction parameters the same. Briefly, ZnO nanostructures were prepared by adding, dropwise, 100 mL of 0.1 M NaOH dissolved in solvent (ethanol, methanol, isopropanol, 1-butanol and double distilled water, separately) into 100 mL of 0.05 M zinc acetate dihydrate ($\text{Zn}(\text{CH}_3\text{COO})_2 \cdot 2\text{H}_2\text{O}$) dissolved in solvent (ethanol, methanol, isopropanol, 1-butanol and double distilled water, separately). These mixtures were irradiated separately under continuous ultrasound (42 kHz) for 2 hours. The white coloured dispersions formed were kept at room temperature for 16 hours to get the precipitates. The as-formed precipitates were washed several times with distilled water to remove the unreacted products. The final products were collected and dried in a hot air oven at 60 °C for 8 hours. The samples were codenamed UE, UM, UI, UB and UW for ethanol, methanol, isopropanol, 1-butanol and water solvents, respectively.

Characterization

The size, shape and morphology of the prepared particles were characterized by high resolution transmission electron microscopy (HR-TEM, FEI TITAN G2 80-300) operated at 300 kV, and transmission electron microscopy (TEM, JEOL Model JSM-6390LV) and the elemental analysis is done using Energy dispersive spectroscopy (JOEL Model JSM-6390LV). To identify the crystalline nature and purity of each sample, the ZnO nanoparticles were investigated by X-ray diffraction (XRD) (Bruker, D4 Endeavor). The X-ray diffractometer used Cu-K α radiation fixed at 40 kV and 30 mA. The measurements were made with an XRD angle (2θ) in the range of 20–80°. The specific surface area of the prepared nanostructures was measured using the Brunauer–Emmett–Teller (BET) method (Flowsorb II 2300 Micrometrics, Inc). Raman spectral measurements were carried out using a micro Raman spectrometer (Jobin-Yvon) with the 532 nm line of an argon ion laser as the exciting light source with 4 mW power. Fourier transform infrared spectroscopy (FTIR) absorption measurements were carried out using a PerkinElmer spectrometer and the KBr pellet technique in the range 4000–400 cm^{-1} . The optical properties of the prepared nanostructures were characterized using absorption spectroscopy and photoluminescence (PL) spectroscopy at room temperature. The UV-visible-NIR spectra were recorded using a Shimadzu dual beam spectrometer in the range 200–900 nm, and the room temperature PL measurements were done using a PerkinElmer fluorimeter at an excitation wavelength of 330 nm.

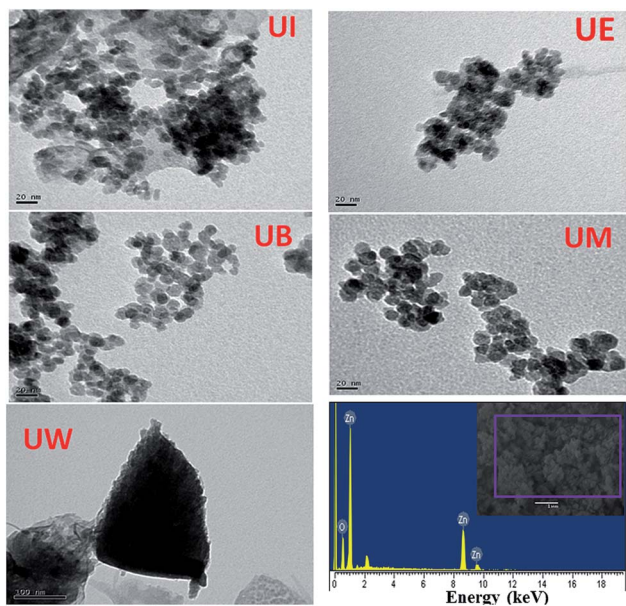


Fig. 1 TEM images of ZnO nanostructures prepared by low frequency ultrasound using various organic solvents (a–f). EDS spectrum of UW sample (g).

Results and discussion

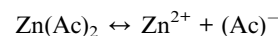
Structural properties

Typical TEM images of the ZnO nanostructures mediated by organic solvents (UI, UE, UB and UM) and water (UW) are presented in Fig. 1. The images reveal that the ZnO nanostructures prepared using an alcohol medium exhibit spherical morphology, whereas water mediated ZnO nanostructures show triangular shaped structures. The particle size distribution is shown in Fig. S2.† Energy-dispersive X-ray spectroscopy (EDS) reveals peaks at 1.01, 8.63, and 9.60 keV which correspond to the Zn, and a peak located at 0.52 keV which is assigned to the oxygen ion. HRTEM images of the ZnO nanostructures are

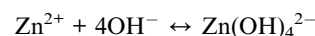
shown in Fig. 2. The images clearly show that the particles are in distorted spherical and hexagonal structures. The ZnO nanostructures prepared using isopropanol and methanol solvents show some hollow pores in the lattice plane, which are of nanometer size.

Based on the experimental results, the various stages involved in the formation of ZnO nanostructures under precipitation conditions are outlined below:³⁶

In the presence of an aqueous medium (organic solvents and water)



The addition of NaOH solution into the zinc acetate solutions causes the reactions



The organic solvents play an important role in the formation of ZnO nanostructures. Spherical particles were obtained when the organic solvents were used to prepare ZnO, and triangular structures were obtained when water was used as a solvent. This is due to the difference in the polarity of the solvents. The water has a stronger polarity than any of the organic solvents; the relatively weak polarity of the organic solvents may limit ZnO growth along the *c*-axis and favour isotropic growth. Similar kinds of results have been reported by Yan *et al.*³⁷ in which ethanol–water mixtures have been used to control the morphologies of ZnO nanostructures. The schematic representation of the growth mechanism is shown in Fig. 3.

Specific surface area (SSA) is one of the important microstructural parameters of materials in determining the nature of

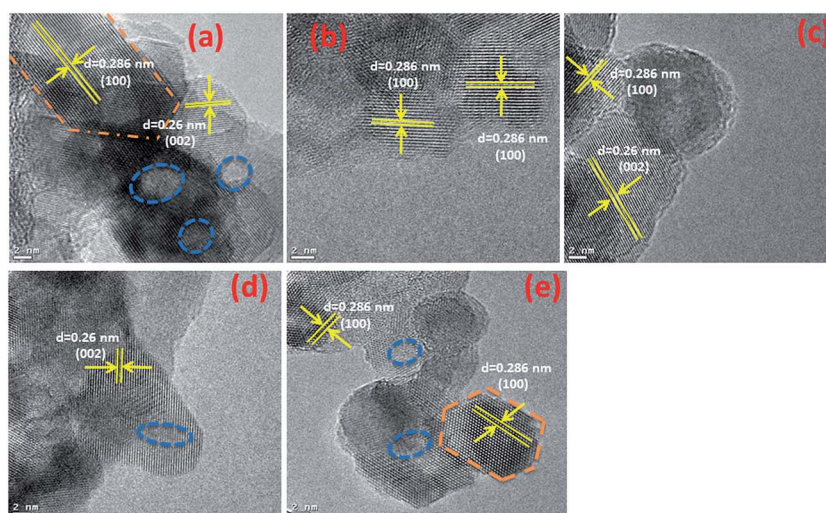


Fig. 2 HRTEM images of prepared ZnO nanostructures (a) UI, (b) UE, (c) UB, (d) UM and (e) UW.

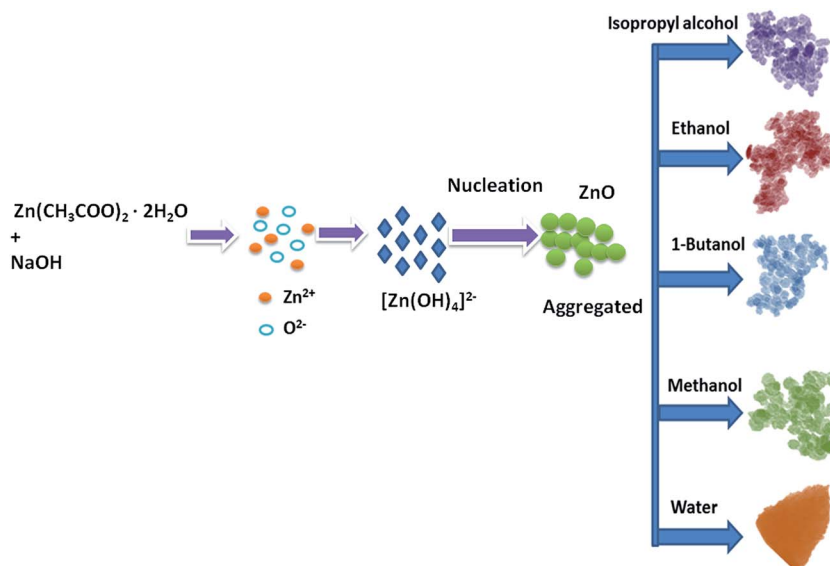


Fig. 3 Schematic illustration of the possible formation process for the ZnO nanostructures.

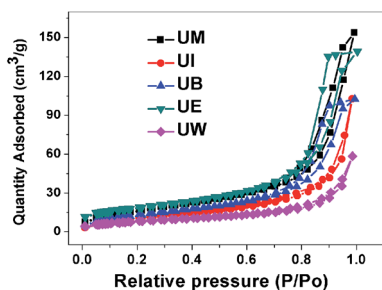


Fig. 4 Nitrogen adsorption-desorption isotherms for the ZnO nanostructures.

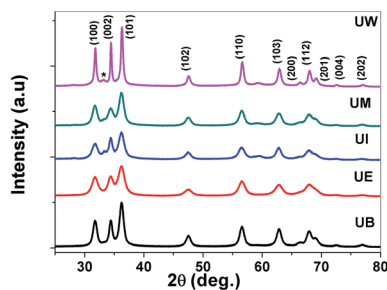


Fig. 5 XRD patterns of the ZnO nanostructures prepared using different solvents. * indicates the zinc hydroxide phase.

porosity, and it is of considerable interest in the fields of catalysis, sensors, filters and pharmaceuticals.³⁸ Fig. 4 represents the nitrogen adsorption-desorption isotherms of the prepared ZnO nanostructures. The obtained values for BET surface areas are 29, 40, 49, 62, 65 $\text{m}^2 \text{g}^{-1}$ corresponding to UW, UI, UB, UM, and UE, respectively; considerable changes have been observed by changing reaction medium.

XRD patterns of the prepared ZnO nanostructures are shown in Fig. 5. All the XRD patterns of ZnO nanostructures show strong and broad peaks which confirm the wurtzite structure of ZnO at the nanoscale. The peaks are located at the angles (2θ) of 31.79° , 34.45° and 36.30° which correspond to the (100), (002) and (101) planes, respectively, of ZnO (JCPDS no: 01-089-1397). The other peaks are found at 2θ angles of 47.57° , 56.63° , 62.91° , 66.39° , 68.01° , 69.14° , 72.51° and 76.86° corresponding to the (102), (110), (103), (200), (112), (201), (004) and (202) planes of the wurtzite structure, respectively. The UI and UW samples show a peak located at 33.1° which corresponds to the zinc hydroxide phase. The broadening of the FWHM was dependent on the size and shape of the nanostructures, and the crystallite size was estimated using the Debye-Scherrer formula.³⁹ The obtained values were found to be ~ 13 , 15, 17, 21, and 38 nm corresponding to UE, UI, UB, UM and UW samples, respectively.

In general, the lattice parameters of semiconductor nanostructures depend on the concentration of dopant ion, structural defects, external strain and the difference of dopant ionic radius with respect to the host matrix ion.³ The lattice parameters, 'a' axis, 'c' axis and unit cell volume 'v', were calculated through the following relations:³⁹

$$a = \frac{\lambda}{\sqrt{3} \sin \theta} (h^2 + hk + k^2) \quad (1)$$

$$c = \frac{\lambda}{\sin \theta} \quad (2)$$

and

$$v = \frac{\sqrt{3}a^2c}{2} \quad (3)$$

The calculated lattice parameters 'a', 'c' and 'v' are shown in Fig. 6(a-c). In the present study, the differences in defects and

microstrain in the samples cause a variation in the lattice constants.

The solvent effect on the ZnO bond length was analysed and is shown in Fig. 6(d). The bond length was calculated by using the relation:⁴⁰

$$L = \sqrt{\left(\frac{a^2}{3}\right) + \left(\frac{1}{2} - u_p\right)^2 c^2} \quad (4)$$

where, 'a', and 'c' are lattice parameters and 'u_p' is the positional parameter which is a measure of the amount by which each atom is displaced with respect to the next, along the 'c' axis. 'u_p' can be calculated by the formula:³

$$u_p = \left(\frac{a^2}{3c^2}\right) + 0.25 \quad (5)$$

The variation of Zn–O bond length in the different solvents is shown in Fig. 6(d).

Microstructural calculations

X-ray profile analysis is a simple and powerful technique to quantify the crystallite size and lattice strain. Williamson–Hall proposed that the broadening of a diffraction line is due to the combination of the crystallite size and strain as a function of the diffraction angle and can be written in the form of a mathematical expression:⁴¹

$$\beta_{hkl} = \beta_t + \beta_\epsilon \quad (6)$$

where, β_t is due to the crystallite size contribution, β_ϵ is due to strain induced broadening and β_{hkl} is the width of the half maximum intensity of the individual diffracted peak. The width of each diffraction line is a combined effect of both instrumental and sample contributions. In order to decompose line broadening effects from the instrumental contribution, a standard silicon (Si) sample was used. The instrumental corrected line broadening of each diffraction peak was calculated through the relation:⁴²

$$\beta_{hkl} = [(\beta_{hkl})_{\text{measured}}^2 - \beta_{\text{instrumental}}]^0.5 \quad (7)$$

where, $\beta_{\text{instrumental}}$ is the broadening due to the instrumental contribution. The diffraction peaks were fitted using the Pearson VII function to calculate the FWHM. The crystallite size (t) contribution can be calculated by using the Scherrer formula:⁴¹

$$\beta_t = \frac{k\lambda}{t \cos \theta} \quad (8)$$

where, k is the shape factor, λ is the wavelength of the X-ray used (0.154056 nm) and β_t is the FWHM of the diffracted peak. Similarly, the strain contribution can be evaluated by the relation:⁴¹

$$\beta_\epsilon = 4\epsilon \tan \theta \quad (9)$$

where, ' ϵ ' is the microstrain. It is clear that the line broadening is a combination of the crystallite size and strain contribution, and it is represented by the mathematical formula:⁴¹

$$\beta_{hkl} = \left(\frac{K\lambda}{t \cos \theta}\right) + (4\epsilon \tan \theta) \quad (10)$$

This can be further simplified as follows:

$$\beta_{hkl} \cos \theta_{hkl} = \left(\frac{K\lambda}{t}\right) + (4\epsilon \sin \theta_{hkl}) \quad (11)$$

The calculated value of $\beta_{hkl} \cos \theta_{hkl}$ as a function of $4 \sin \theta_{hkl}$ is plotted and is shown in ESI Fig. 3.† This model is known as the uniform deformation model (UDM).

In UDM, microstrain (ϵ) is assumed to be isotropic (uniform in all the crystallographic directions), but this assumption is no longer valid since the microstructural properties vary with the crystallographic directions. Microstrain can be correlated with stress, which is directionally dependent. In the uniform deformation stress model (UDSM), the uniform deformation stress (σ) is expressed as:

$$\sigma = E_{hkl}\epsilon_{hkl} \quad (12)$$

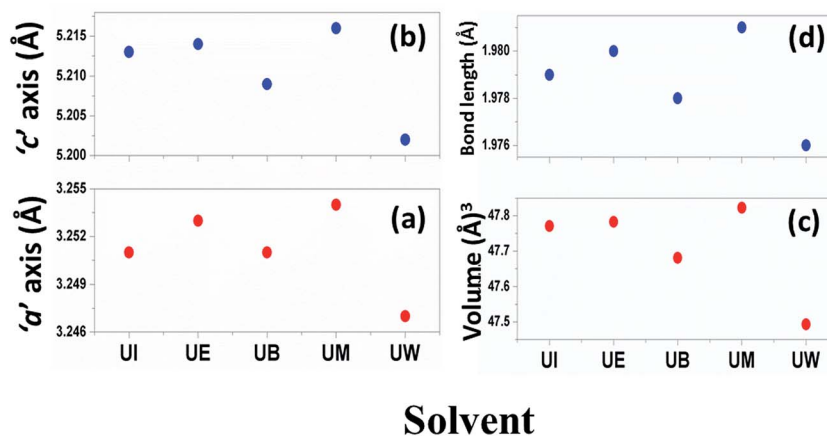


Fig. 6 Variations of lattice parameters with the different solvents: (a) 'a' axis; (b) 'c' axis; (c) unit cell volume; and (d) bond length.

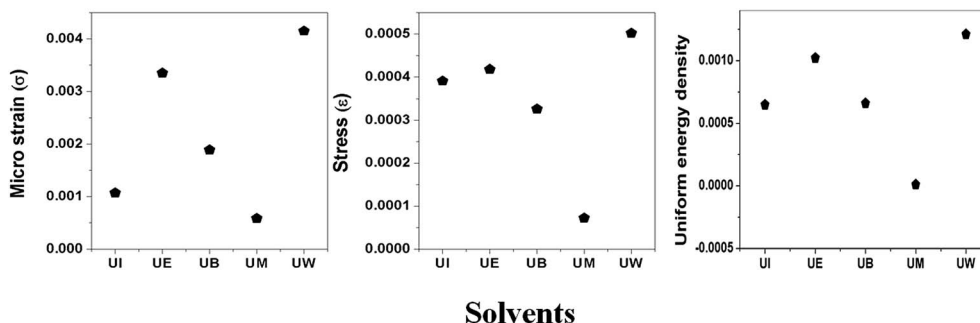


Fig. 7 Variation of microstrain, stress, and uniform energy density with the different solvents.

where, E_{hkl} is the Young's modulus in the direction perpendicular to the (hkl) plane and ε_{hkl} is the anisotropic microstrain, dependent on the crystallographic directions. For the hexagonal crystals, the Young's modulus could be obtained through the following relation:⁴³

$$E_{hkl} = \frac{\left[h^2 + \frac{(h+2k)^2}{3} + \left(\frac{a}{c}l\right)^2 \right]}{S_{11} \left(h^2 + \frac{(h+2k)^2}{3} \right) + S_{33} \left(\frac{a}{c}l\right)^4 + (2S_{13} + S_{44}) \left(h^2 \frac{(h+2k)^2}{3} \right) \left(\frac{a}{c}l\right)^2} \quad (13)$$

where, 'a' and 'c' are lattice parameters and S_{11} , S_{33} , S_{13} and S_{44} are the elastic compliances of ZnO. The values of the elastic compliances are 7.858×10^{-12} , -2.206×10^{-12} , 6.940×10^{-12} and 23.57×10^{-12} respectively.⁴⁴ In the UDSM model, the W-H equation becomes:

$$\beta_{hkl} \cos \theta_{hkl} = \left(\frac{K\lambda}{t} \right) + \left(\frac{4\sigma \sin \theta_{hkl}}{E_{hkl}} \right) \quad (14)$$

σ can be obtained estimated from the slope of the linear fit of the graph which is plotted between $\beta_{hkl} \cos \theta_{hkl}$ and $4 \sin \theta/E_{hkl}$, and is shown in ESI Fig. 4.† Fig. 7 depicts the variation of microstrain and stress with the solvents. Similarly, the Young's modulus and ε_{hkl} are connected to the density of deformation energy 'u' through the relation:⁴²

$$\varepsilon_{hkl} = \left(\frac{2u}{E_{hkl}} \right)^{1/2} \quad (15)$$

Substituting eqn (15) into eqn (11), the W-H relation becomes:

$$\beta_{hkl} \cos \theta_{hkl} = (2^{5/2} \sin \theta_{hkl} E_{hkl}^{-1/2}) u^{1/2} \quad (16)$$

The value 'u' can be obtained from the plot between $2^{5/2} \sin \theta_{hkl} E_{hkl}^{-1/2}$ vs. $\beta_{hkl} \cos \theta_{hkl}$ which is shown in ESI Fig. 5,† and the value of uniform energy density is shown in Fig. 7. This model is known as the uniform deformation energy density model (UDEDM).

Vibrational properties

Raman spectra. Raman spectroscopy is a non-destructive testing tool used to study the vibrational properties of bulk/nanostructured materials, and specifically to identify dopant ions in the lattice plane, secondary phase formation, and structural disorder properties of nanostructures.⁴⁵ Wurtzite type ZnO is a II-VI wide band gap semiconductor belonging to the space group C_{6v}^4 , with two formula units in the primitive cell.³² According to group theory analysis, the zone centre optical phonons can be classified to the following irreducible representation: $\Gamma_{opt} = A_1 + E_1 + 2E_2 + 2B_1$, where A_1 and E_1 modes are polar modes and both Raman and infrared active, and they can split into transverse optical (TO) and longitudinal optical (LO) phonons. The Raman active phonon of the A_1 branch is polarized in the z-direction, whereas the E_1 branch is polarized in the xy plane.³³ E_2 modes are only Raman active, non-polar modes and they have two wavenumbers, one with low frequency (E_2^{low}) associated with the vibrations of the Zn sub-lattice and one with high frequency (E_2^{high}) associated with the motion of oxygen atoms only. The B_1 modes are both Raman and infrared inactive and are known to be silent modes.

In order to investigate the influence of size and shape on the Raman scattering of ZnO nanostructures, the room temperature non-resonant Raman scattering of all samples was measured in the range 50 to 2000 cm^{-1} and the spectra are shown in Fig. 8(a-e). According to DFT calculations, the second order phonon modes are divided into three regions: (i) the frequency range

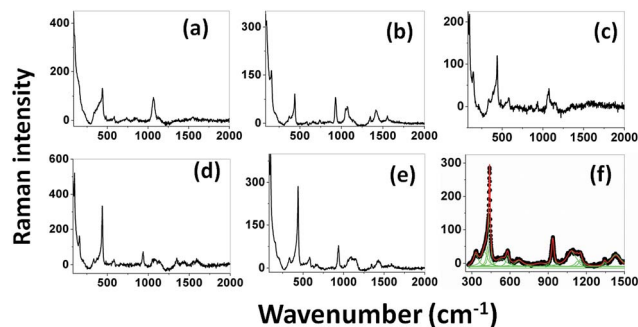


Fig. 8 Room temperature non resonant Raman spectra of UE (a), UI (b), UW (c), UM (d), and UB (e) ZnO nanostructures. Lorentzian decomposed Raman spectrum of UB sample (f).

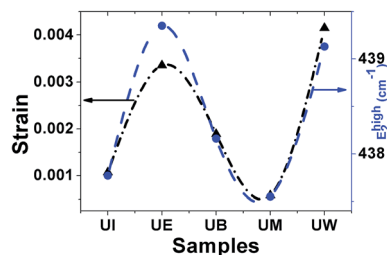


Fig. 9 Variation of microstrain vs. the E_2^{high} mode.

between 160 and 540 cm^{-1} is associated with acoustic overtones, (ii) the frequency range between 540 and 820 cm^{-1} is attributed to the combinations of optical and acoustic phonon modes, and (iii) the high frequency region between 820 and 1120 cm^{-1} is formed by optical overtones and combinations.³² To identify the individual phonon modes, each Raman spectrum was fitted using the Lorentzian function and the decomposed spectrum of the UB sample is shown in Fig. 7(f). The characteristic Raman bands of the wurtzite ZnO lattice, located at 98 and 437 cm^{-1} , are assigned to E_2^{low} and E_2^{high} respectively. The band appearing at $\sim 330\text{ cm}^{-1}$ is ascribed to the difference $E_2^{\text{high}} - E_2^{\text{low}}$ which is known to be due to multiphonon scattering. The peaks at 532 , 547 , and 551 cm^{-1} are clearly of A_1 symmetry and can be attributed to the $2B_1^{\text{low}}$ and LA overtones. The reason for the observation of B_1 silent modes and second order phonon modes are due to the breakdown of the translational symmetry of the lattice caused by defects or impurities which arise because of either the dopant nature or the growth conditions.³⁰ The phonon modes located at 699 , 732 , and 755 cm^{-1} can be ascribed to the combinations of acoustic and optical phonons of A_1 symmetry. Similarly, a three phonon combination mode, appearing in the higher frequency region at

$\sim 1431\text{ cm}^{-1}$, is ascribed to the A_1 (long) + E_1 (transv) + E_2 process.³⁵ Two phonon combinations modes, located at 679 and $\sim 835\text{ cm}^{-1}$, could be assigned to the vibrations of A_1 (long) + E_2 and E_1 (transv) + E_2 respectively. The second order multiphonon scattering mode, appearing at $\sim 935\text{ cm}^{-1}$, could be assigned to the vibrations from $2E_{2\text{H}} + E_{2\text{L}}$. The phonon frequency observed at higher wavenumber is known to be from a second order Raman process; in the present case, the peak observed at $\sim 1140\text{ cm}^{-1}$ is assigned to the 2LO vibrations. Fig. 9 represents the variations of microstrain and the E_2^{high} mode in the different samples. In general, the E_2^{high} mode is highly sensitive to the lattice strain. The increase of the lattice parameter c leads to tensile strain along the c -axis which causes a blue shift, and similarly a decrease of the lattice parameter c causes a compressive strain along the c -axis which results in a red shift of the E_2^{high} phonon mode (Table 1).³¹

Phonon life time. The phonon life time (τ) can be deduced from the Raman scattering by using the energy–time uncertainty relation $\frac{1}{\tau} = \frac{\Delta E}{\hbar} = 2\pi c\Gamma$ where, ΔE is the uncertainty in the energy of the phonon mode, \hbar is the Planck constant, and Γ is the FWHM of the Raman modes in cm^{-1} .³² The phonon life time is a combination of two characteristic decay times such as the anharmonic decay of the phonon into two or more phonons so that energy and momentum are conserved (τ_A) and the perturbation of the translational symmetry of the crystals due to the presence of impurities, defects and isotopic fluctuations (τ_I). Thus the calculated phonon life time is an addition of these two characteristics decay times $\left[\frac{1}{\tau} = \frac{1}{\tau_A} + \frac{1}{\tau_I}\right]$. The calculated phonon life time values are listed in Table 2.

FTIR spectra. The recorded FTIR spectra of the prepared ZnO nanostructures are displayed in Fig. 10. Usually in inorganic species, the vibrational motions lie in the wavenumber range

Table 1 Phonon vibrational bands, assignments and symmetries of the first order, second order and multiphonon Raman scattering of the ZnO nanostructures^a

UE, cm^{-1}	UI, cm^{-1}	UM, cm^{-1}	UB, cm^{-1}	UW, cm^{-1}	Ref.	Symmetry	Process
99	98	98	99	98	99	E_2	E_2^{low}
339	333	330	330	334	333	$A_1, (E_2, E_1)$	$E_2^{\text{high}} - E_2^{\text{low}}$
376	375	386	399	396	378	A_1	A_1 (TO)
413	420	421	423	423	410	E_1	E_1 (TO)
439	437	437	438	439	438	E_2	E_2^{high}
483	—	483	—	484	483	A_1	2LA
551	—	—	532	547	541	A_1	$2B_1^{\text{low}}$; 2LA
—	576	574	579	—	574	A_1	A_1 (LO)
582	—	—	—	581	584	E_1	E_1 (LO)
—	—	—	669	—	666	A_1	TA + LO
—	—	—	—	679	679	Two phonon combinations	A_1 (long) + E_2
—	—	699	—	—	700	A_1	LA + TO
732	755	—	—	—	745	A_1	LA + TO
847	—	—	835	859	845	Two phonon combinations	E_1 (transv) + E_2
—	930	934	935	932	950	Second order multiphonon scattering	$2E_{2\text{H}} + E_{2\text{L}}$
—	1050	—	—	—	1044	A_1	TO + LO
1067	1073	1074	1080	1068	1072	A_1	TO + LO
1139	1122	1140	1154	1144	1158	A_1	$2A_1$ (LO); $2E_1$ (LO); 2LO
—	1421	1444	1431	1432	1425	Three phonon combinations	A_1 (long) + E_1 (transv) + E_2

^a Our results are compared to the Raman wavenumbers taken from Cusco *et al.*,³² and Kunert *et al.*³⁵

Table 2 Phonon life time measurements for ZnO nanostructures

Phonon mode	UE		UI		UM		UB		UW	
	Γ (cm ⁻¹)	τ (ps)								
E ₂ ^{low}	7.92	0.67	7.37	0.719	7.83	0.677	7.81	0.679	6.667	0.795
E ₂ ^{high} – E ₂ ^{low}	19.56	0.271	9.11	0.582	28.84	0.1839	45.94	0.1154	24.87	0.213
A ₁ (TO)	43.61	0.121	58.12	0.091	73.94	0.071	52.75	0.1005	102.565	0.052
E ₁ (TO)	42.62	0.124	27.68	0.192	27.78	0.191	25.57	0.207	34.69	0.1528
E ₂ ^{high}	16.08	0.329	11.6	0.457	11.45	0.463	11.85	0.447	12.09	0.438
2LA	4.08	1.301	—	—	4.39	1.208	—	—	7.939	0.668
2B ₁ ^{low} ; 2LA	35.6	0.148	—	—	—	—	93.45	0.056	92.74	0.057
A ₁ (LO)	—	—	16.588	0.319	28.91	0.183	27.07	0.196	—	—
E ₁ (LO)	12.57	0.422	—	—	—	—	—	—	22.41	0.237
2E _{2H} + E _{2L}	—	—	17.81	0.297	21.38	0.248	21.76	0.244	13.33	0.398
TO + LO	37.37	0.142	29.01	0.183	71.95	0.073	90.81	0.058	46.46	0.114
2A ₁ (LO); 2E ₁ (LO); 2LO	21.15	0.25	66.89	0.079	51.36	0.103	41.4	0.128	60.89	0.087
A ₁ (long) + E ₁ (transv) + E ₂	—	—	63.06	0.084	180.19	0.029	65.27	0.055	378.8	0.014

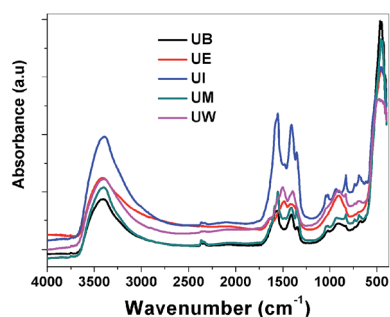


Fig. 10 FTIR spectra of the ZnO nanostructures prepared using different solvents.

<600 cm⁻¹, and vibrational motion at higher wavenumbers can be assigned to organic species. All the spectra show an absorbance band at ~460 cm⁻¹ which is assigned to the E₁ (TO) mode vibrations of ZnO.³⁹ The broad bands at around ~3400 and ~1620 cm⁻¹ could be assigned to the stretching and bending vibrations of H–O–H bonds, respectively.⁴⁶ The bands observed at ~1350–1450 and ~1550 cm⁻¹ are assigned to the symmetric and asymmetric stretching vibrations of COO⁻ modes from the carboxyl groups of the acetate in the metal precursors.

Optical properties

Absorption spectra. The optical absorption spectra of the samples prepared using various solvents are shown in Fig. 11(a). The peaks appearing at 3.422, 3.576, 3.58, 3.601 and 3.622 eV correspond to the samples UW, UM, UB, UE and UI respectively, and are due to the free excitonic absorption of the ZnO nanostructures. All the samples exhibit an excitonic peak shift as compared with the bulk ZnO absorption (3.37 eV) which is due to the quantum confinement effect. The ESI Fig. 5† clearly shows that there is band gap tuning due to the variation in the particle size. Previous reports have revealed that the band structure of the ZnO is size dependent and the particle size strongly influences the energetic position of the band edges.² The band gap is inversely proportional to the size of the particles through the relation:²

$$E = E_g + \frac{h^2}{8R^2} \left(\frac{1}{m_e^*} + \frac{1}{m_h^*} \right) - \frac{1.8e^2}{4\pi\epsilon_0\epsilon_\infty R} \quad (17)$$

where, E_g is the bulk band gap, R is the particle size, m_e^* is the effective mass of the electron, m_h^* is the effective mass of the hole, ' e ' is the charge of the electron and ' ϵ_∞ ' is the high frequency dielectric constant. The correlation of the calculated band gap values *versus* particle size using eqn (17) is shown in

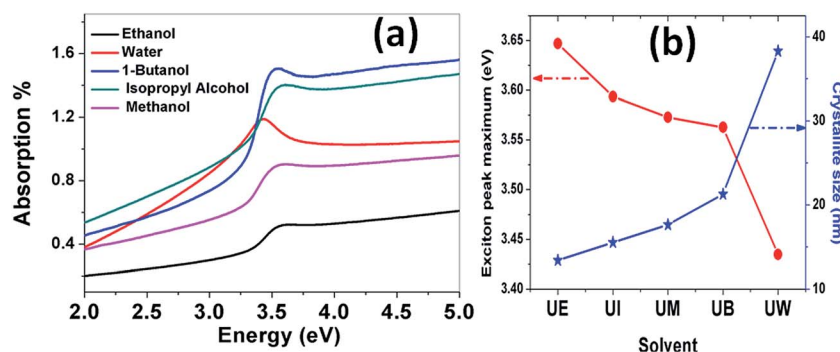


Fig. 11 (a) Absorption spectra of the ZnO nanostructures prepared using different solvents. (b) Variation of the exciton peak maximum and crystallite size as a function of the solvent.

ESI Fig. 4,[†] and this reveals the shifts in the band edges as a function of particle size. The variation of the excitonic peak maximum and crystallite size in the different solvents is shown in Fig. 11(b). This clearly shows that the band edge varies with respect to the particle size.

Photoluminescence spectra. In general, ZnO nanostructures have two emission bands, the relatively weak and narrow ultra violet (UV) emission band and the much stronger, broader emission band located at around 400–600 nm.⁴⁷ Several works both theoretically and experimentally have reported the mechanism behind the origin of the broad visible emission from ZnO.⁴⁸ The origin of the visible emission is due to the recombination of a photogenerated electron from a shallow level which is very close to the conduction band with the deep traps in the single ionized oxygen vacancy sites and/or the single negatively charged interstitial oxygen ions. This visible emission has a longer life time than the UV emission, in the order of microseconds.⁴⁹ The UV emission band arises due to the radiative annihilation of excitons and the life time of this emission is very short, in the order of picoseconds. The PL spectra of ZnO nanostructures prepared using different solvents are shown in Fig. 12(a). The spectra show two emission bands, the first at around 385 nm, with low intensity, and the second centred at ~530 nm with a broad band. These are assigned to the near band edge emission (NBE) and visible emission, respectively. The relative intensity of the visible to the UV emission ($I_{\text{vis}}/I_{\text{UV}}$) strongly depends on the size of the particles, as shown in Fig. 12(b).

The variation of intensity ratio of visible to UV emission is indicated in Fig. 12(b). It is clear that the ZnO nanoparticles prepared using isopropanol show a much higher intensity for the visible emission band than the exciton emission band. Interestingly, the visible emission band is gradually decreased for the samples prepared using ethanol, 1-butanol, and methanol and is completely absent for the UW samples. This phenomenon can be explained using size effects. The band appearing below the conduction band edge (2 eV) is assumed to be the recombination centre V_{o}^+ for the visible emission. The recombination of a conduction band electron with a V_{o}^{++} centre can yield a photon with energy of 2 eV. The V_{o}^{++} centre can be created by the trapping of a hole in the V_{o}^+ centre, and the probable hole trapping site is on the surface of the particles.⁵⁰ When the particle possesses a large surface to volume ratio, efficient and fast trapping of photogenerated holes results at

surface sites. The rate of the surface trapping process and defect concentration decreases as the particle size increases due to the decrease of surface to volume ratio.⁴⁸ In the present case, the UI sample exhibits a high intensity visible emission band, this is gradually decreased for UE, UB and UM and is completely absent for UW samples. This is because of the reduction of possible trapping surface sites which results in the decrease of visible emission band intensity.

Conclusion

In summary, ZnO nanostructures were prepared by the low frequency (42 kHz) ultrasound route using various organic solvents as the reaction media. Lattice and microstructural parameters such as microstrain, stress, and energy density of the prepared ZnO nanostructures were extracted from X-ray diffraction (XRD) analysis. TEM images revealed morphological changes involving a spherical to triangular shaped structure, and the size of the nanoparticles was found to be dependent on the organic solvent used. Raman spectral measurements revealed that the changes in the phonon mode are due to the variation of microstrain and the presence of multiphonon scattering. The intensity of the visible emission band was found to vary with the particles' size and morphology. The strongest visible emission band corresponded to the smallest size with the largest surface/volume ratio. This could be attributed to the trapping of surface oxygen vacancies.

Acknowledgements

The authors gratefully acknowledge the FONDECYT-CONICYT (Projects No: 3140178 and No. 1130916) Government of Chile, Santiago, for financial assistance.

References

- 1 C. F. Klingshirm, A. Waag, A. Hoffmann and J. Geurts, *Zinc Oxide: From Fundamental Properties Towards Novel Applications*, Springer, Heidelberg, Dordrecht, Lodon, New York, 2010, ISBN 978364210577-7.
- 2 A. van Dijken, E. A. Meulenkaamp, D. Vanmaekelbergh and A. Meijerink, *J. Phys. Chem. B*, 2000, **104**, 1715–1723.
- 3 Ü. Özgür, Y. I. Alivov, C. Liu, A. Teke, M. A. Reshchikov, S. Doan, V. Avrutin, S.-J. Cho and H. Morkoç, *J. Appl. Phys.*, 2005, **98**, 041301.
- 4 D. Costenaro, F. Carniato, G. Gatti, L. Marchese and C. Bisio, *New J. Chem.*, 2013, **37**, 2103–2109.
- 5 W. J. E. Beek, M. M. Wienk and R. A. J. Janssen, *Adv. Mater.*, 2004, **16**, 1009–1013.
- 6 M. Chen, L. Hu, J. Xu, M. Liao, L. Wu and X. Fang, *Small*, 2011, **7**, 2449–2453.
- 7 B. Zhao, F. Wang, H. Chen, Y. Wang, M. Jiang, X. Fang and D. Zhao, *Nano Lett.*, 2015, **15**, 3988–3993.
- 8 D. Jassby, J. F. Budarz and M. Wiesner, *Environ. Sci. Technol.*, 2012, **46**, 6934–6941.
- 9 V. Chivukula, D. Ciplis, M. Shur and P. Dutta, *Appl. Phys. Lett.*, 2010, **96**, 233512.

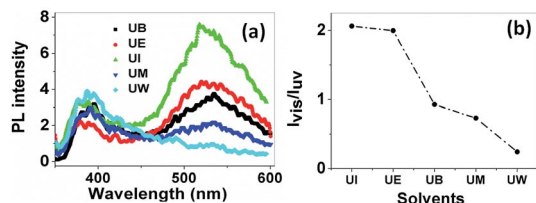


Fig. 12 (a) PL spectra of the prepared samples at an excitation wavelength of 330 nm. The band at 385 nm is from near band edge emission, and the broad band at 530 nm is due to deep level trap emission. (b) The relative intensity variation of visible to UV emission with respect to the solvents.

- 10 K. R. Raghupathi, R. T. Koodali and A. C. Manna, *Langmuir*, 2011, **27**, 4020–4028.
- 11 L. Xu, Y. L. Hu, S. Sithambaram, C. Pelligra, M. Aindow, C. H. Chen, R. Joesten, L. Jin, H. Huang and S. L. Suib, *Chem. Mater.*, 2009, **21**, 2875–2885.
- 12 B. Cheng and E. T. Samulski, *Chem. Commun.*, 2004, **986**, 986–987.
- 13 X. Zhao and L. Qi, *Nanotechnology*, 2012, **23**, 235604.
- 14 R. Siddheswaran, R. V. Mangalaraja, Ricardo E. Avila, D. Manikandan, C. Esther Jeyanthi and S. Ananthakumar, *Mater. Sci. Eng., A*, 2012, **558**, 456–461.
- 15 A. K. Zak, W. H. abd Majid, H. Z. Wang, R. Yousefi, A. M. Golsheikh and Z. F. Ren, *Ultrason. Sonochem.*, 2013, **20**, 395–400.
- 16 S. Baruah and J. Dutta, *J. Cryst. Growth*, 2009, **311**, 2549–2554.
- 17 H. Zhang, D. Yang, X. Ma, Y. Ji, J. Xu and D. Que, *Nanotechnology*, 2004, **15**, 622–626.
- 18 A. C. Cakir and S. E. Ela, *Adv. Powder Technol.*, 2012, **23**, 655–660.
- 19 S. K. Na Ayudhya, P. Tonto, O. Mekasuwandumrong, V. Pavarajarn and P. Praserthdam, *Cryst. Growth Des.*, 2006, **6**, 2446–2450.
- 20 J. M. Patete, X. Peng, C. Koenigsmann, Y. Xu, B. Karn and S. S. Wong, *Green Chem.*, 2011, **13**, 482–519.
- 21 M. Ghosh, D. Karmakar, S. Basu, S. N. Jha, D. Bhattacharyya and S. C. G. Gupta, *J. Phys. Chem. Solids*, 2014, **75**, 543–549.
- 22 C. R. Chandraiahgari, G. D. Bellis, P. Ballirano, S. K. Balijepalli, S. Kaciulis, L. Caneve, F. Sarto and M. S. Sarto, *RSC Adv.*, 2015, **5**, 49861–49870.
- 23 G. Clavel, M. G. Willinger, D. Zitoun and N. Pinna, *Adv. Funct. Mater.*, 2007, **17**, 3159–3169.
- 24 Q. R. Hu, S. L. Wang, P. Jiang, H. Xu, Y. Zhang and W. H. Tang, *J. Alloys Compd.*, 2010, **496**, 494–499.
- 25 K. L. Foo, M. Kashif, U. Hashim and W. W. Liu, *Ceram. Int.*, 2014, **40**, 753–761.
- 26 X. Fang, L. Hu, C. Ye and L. Zhang, *Pure Appl. Chem.*, 2010, **82**, 2185–2198.
- 27 T. Andelman, G. Neumark, Y. Gong, M. Polking, S. O. Brien, M. Yin and I. Kuskovsky, *J. Phys. Chem. B*, 2005, **109**, 14314–14318.
- 28 C. Ye, X. Fang, Y. Hao, X. Teng and L. Zhang, *J. Phys. Chem. B*, 2005, **109**, 19758–19765.
- 29 A. Pimentel, J. Rodrigues, P. Duarte, D. Nunes, F. M. Costa, T. Monteiro, R. Martins and E. Fortunato, *J. Mater. Sci.*, 2015, **50**, 5777–5787.
- 30 F. J. Manjon, B. Mari, J. Serrano and A. H. Romero, *J. Appl. Phys.*, 2005, **97**, 53516.
- 31 M. Scepanovic, M. G. Brojcin, K. Vojisavljevic, S. Bernik and T. Sreckovic, *J. Raman Spectrosc.*, 2010, **41**, 914–921.
- 32 R. Cuscó, E. Alarcón-Lladó, J. Ibáñez and L. Artús, *Phys. Rev. B: Condens. Matter Mater. Phys.*, 2007, **75**, 165202.
- 33 H. K. Yadav, K. Sreenivas, R. S. Katiyar and V. Gupta, *J. Phys. D: Appl. Phys.*, 2007, **40**, 6005–6009.
- 34 R. S. Zeferino, M. B. Flores and U. Pal, *J. Appl. Phys.*, 2011, **109**, 014308 (1–6).
- 35 H. W. Kunert, D. J. Brink, F. D. Auret, J. Malherbe, J. Barnas and V. Kononenko, *Phys. Status Solidi C*, 2005, **2**, 1131–1136.
- 36 Y. F. Zhu, G. H. Zhou, H. Y. Ding, A. H. Liu, Y. B. Lin and N. L. Li, *Phys. E*, 2010, **42**, 2460–2465.
- 37 Z. Yan, Y. Ma, D. Wang, J. Wang, Z. Gao and T. Song, *J. Phys. Chem. C*, 2008, **112**, 9219–9222.
- 38 J. Becker, K. R. Raghupathi, J. S. Pierre, D. Zhao and R. T. Koodali, *J. Phys. Chem. C*, 2011, **115**, 13844–13850.
- 39 C. Suryanarayana and M. Grant Norton, *X-ray diffraction: a practical approach*, Plenum Press, New York, 1998, p. 213.
- 40 X. S. Wang, Z. C. Wu, J. F. Webb and Z. G. Liu, *Appl. Phys. A*, 2003, **77**, 561–565.
- 41 V. Biju, N. Sugathan, V. Vrinda and S. L. Salini, *J. Mater. Sci.*, 2008, **43**, 1175–1179.
- 42 Y. Rosenberg, V. S. Machavariani, V. Voronel, S. Garber, A. Rubshtein, A. I. Frenkel and E. A. Stern, *J. Phys.: Condens. Matter*, 2000, **12**, 8081–8088.
- 43 J. M. Zhang, V. Zhanga, K. W. Xub and V. Jic, *Solid State Commun.*, 2006, **139**, 87–91.
- 44 J. F. Nye, *Physical properties of crystals: their representation by tensors and matrices*, New York, Oxford, 1985.
- 45 T. Pandiyarajan and B. Karthikeyan, *J. Raman Spectrosc.*, 2013, **44**, 1534–1539.
- 46 T. Gruber, G. M. Prinz, C. Kirchner, R. Kling, F. Reuss, W. Limmer and A. Waag, *J. Appl. Phys.*, 2004, **96**, 289–293.
- 47 A. Sahai and N. Goswami, *Phys. E*, 2014, **58**, 130–137.
- 48 A. B. Djuricic and Y. H. Leung, *Small*, 2006, **2**, 944–961.
- 49 A. van Dijken, E. A. Meulenkaamp, D. Vanmaekelbergh and A. Meijerink, *J. Phys. Chem. B*, 2000, **104**, 1715–1723.
- 50 A. van Dijken, E. A. Meulenkaamp, D. Vanmaekelbergh and A. Meijerink, *J. Lumin.*, 2000, **90**, 123–128.